

Cavity optomechanics with sub-wavelength grating mirrors

This article has been downloaded from IOPscience. Please scroll down to see the full text article.

2012 New J. Phys. 14 125010

(<http://iopscience.iop.org/1367-2630/14/12/125010>)

View [the table of contents for this issue](#), or go to the [journal homepage](#) for more

Download details:

IP Address: 129.6.128.44

The article was downloaded on 27/12/2012 at 21:10

Please note that [terms and conditions apply](#).

Cavity optomechanics with sub-wavelength grating mirrors

Utku Kemiktarak^{1,2,3}, Mathieu Durand¹, Michael Metcalfe^{1,2,4}
and John Lawall^{1,5}

¹ National Institute of Standards and Technology, 100 Bureau Drive,
Gaithersburg, MD 20899, USA

² Joint Quantum Institute, University of Maryland, College Park, MD 20742,
USA

E-mail: john.lawall@nist.gov

New Journal of Physics **14** (2012) 125010 (22pp)

Received 30 May 2012

Published 18 December 2012

Online at <http://www.njp.org/>

doi:10.1088/1367-2630/14/12/125010

Abstract. We design, fabricate and study a novel platform for cavity optomechanics: a silicon nitride membrane patterned as a sub-wavelength diffraction grating. Using the grating as one mirror of a Fabry–Perot cavity, we realize an optical finesse of $F = 2830 \pm 60$, corresponding to a grating reflectivity of $R = 0.998$. The finesse we achieve appears to be within a factor of two of the limit set by material absorption. We study the finesse as a function of wavelength and optical spot size in order to elucidate various optical loss mechanisms. We find that the cavity exhibits birefringence, and establish that it, too, is a source of optical loss. We then characterize the mechanical motion. We observe hundreds of normal modes, and find the fluctuating amplitude of one of them to be very well described by a Boltzmann distribution. By injecting a red-detuned cooling laser, we optically cool all of the modes that we observe. The lowest effective temperature we achieve is $T_{\text{eff}} \approx 1$ K.

³ The first two authors contributed equally to this work.

⁴ Present address: Booz Allen Hamilton.

⁵ Author to whom any correspondence should be addressed.



Content from this work may be used under the terms of the [Creative Commons Attribution-NonCommercial-ShareAlike 3.0 licence](https://creativecommons.org/licenses/by-nc-sa/3.0/). Any further distribution of this work must maintain attribution to the author(s) and the title of the work, journal citation and DOI.

Contents

1. Introduction	2
2. Optical properties of sub-wavelength grating mirrors	3
2.1. Infinite size grating; plane-wave illumination	4
2.2. Confined optical mode	6
3. Experiment	7
3.1. Device fabrication	7
3.2. Cavity	8
4. Optical characterization	9
4.1. Transmission, reflection, finesse	9
4.2. Spatial mode size	11
4.3. Polarization	13
5. Mechanical characterization	15
5.1. Passive mechanical characterization	15
5.2. Optical cooling	18
6. Conclusion and outlook	19
Acknowledgments	21
References	21

1. Introduction

Cavity optomechanics is at this point a mature research field, in which many different platforms have been demonstrated which couple the energy in a mechanical resonator to the energy stored in an optical cavity [1]. The ideal optomechanical system combines low optical and mechanical losses, low mass, and strong coupling between the optical and mechanical degrees of freedom. While it is difficult to realize all of these criteria simultaneously, a hybrid ‘membrane-in-the-middle’ Fabry–Perot cavity largely does so. In this platform, a thin silicon nitride (SiN) membrane, functioning as a high- Q mechanical resonator with low optical loss, is placed within a high-finesse optical cavity comprised of two conventional highly-reflective dielectric mirrors. When first demonstrated [2], this system achieved an unprecedented optical cooling efficiency despite the low reflectivity ($R = 0.18$) of the SiN membrane, a consequence of the very low losses that were realized. Substantially lower mechanical and optical losses were subsequently demonstrated in such a system by the use of stoichiometric silicon nitride, Si_3N_4 [3].

From the outset it was recognized that certain experiments, such as the observation of mechanical quantum jumps, would be possible in such systems only with membranes of considerably higher reflectivity. As interest developed in experiments employing multiple membranes within a cavity [4–6], other potential benefits of stronger optomechanical coupling became evident. Multiple highly-reflective membranes can be used to increase the effective cavity length [6], for example, thus placing optomechanical systems with low mechanical frequencies and large optical linewidths in the resolved-sideband regime required for ground-state cooling.

Remarkably, there is a well-established method to increase the reflectivity of a dielectric membrane to nearly unity, while in fact reducing its mass, which is to remove material so as to

pattern it as a diffraction grating with a sub-wavelength period. Such devices have been used in vertical cavity surface emitting lasers [7], where the inferred reflectivity was $R = 0.995$. They have recently been demonstrated in devices designed as optomechanical systems. A reflectivity of $R = 0.95$ was demonstrated in a mechanically compliant device with resonances in the MHz range [8], and in our early work we obtained [9] a reflectivity of $R = 0.994$ in a patterned SiN membrane, accompanied by a mechanical mode having a quality factor of $Q = 7.5 \times 10^5$.

In this work, we explore the use of a sub-wavelength grating patterned in SiN as an optomechanical element in considerably more detail. We start by establishing a region of parameter space amenable to fabricating a grating with near-unity reflectivity, and calculate the limiting reflectivity set by material absorption. We fabricate these devices and incorporate one of them as an end mirror in a standard two-mirror Fabry–Perot cavity. We measure a finesse as large as $F = 2830 \pm 60$, and explore various optical loss mechanisms related to the geometry of the confined mode and the wavelength. We find a clear signature of birefringence in the cavity and discuss its consequences. We then illustrate the mechanical properties of these devices. The mechanical quality factor is not severely degraded by fabrication of the grating, and we realize optical cooling from room temperature to an effective temperature of $T_{\text{eff}} \approx 1$ K.

All of the results presented here are made with a conventional two-mirror cavity. The results we obtain, however, should be relevant to work in which these highly-reflective membranes are used in a ‘membrane in the middle’ cavity. At the same time, the two-mirror cavity is interesting in its own right; it is a far simpler system requiring less alignment, and a next-generation two-mirror cavity incorporating a grating membrane should be capable of reaching the resolved-sideband regime required for optical cooling to the mechanical ground state [10, 11].

2. Optical properties of sub-wavelength grating mirrors

The operating principle of sub-wavelength grating mirrors has been discussed thoroughly in the literature, and a comprehensive review has recently appeared [12]. Briefly, when a diffraction grating with period a is illuminated at normal incidence by means of a plane wave of wavelength λ , diffracted beams appear at angles θ_m given by $\sin\theta_m = m\lambda/a$, where the order number m is an integer. The distribution of power among the diffracted orders depends on the details of the grating, and it has long been known that by appropriately ‘blazing’ the grating, it is possible to optimize the amount of light scattered into a desired order. If the grating periodicity is smaller than the wavelength, $a < \lambda$, it is readily seen that the only diffracted orders that are allowed correspond to $m = 0$, either transmitted or reflected at normal incidence. By appropriate design of the grating, it is possible to force nearly all of the scattered light into the reflected beam. While superficially resembling blazing, the phenomenon is better described as destructive interference between the directly-transmitted beam and radiation modes that are coupled to leaky guided modes of the grating structure [13–17].

Sub-wavelength grating mirrors have been demonstrated in a variety of material systems. The simplest platform, and probably the one most suitable for cavity optomechanics, is shown in figure 1(a). It consists of a dielectric slab with an index of refraction n that is perforated with lines or holes, giving an index contrast of $n:1$. One-dimensional gratings comprised of a periodic array of rectangular segments separated by air have been demonstrated using InP ($n = 3.17$) [18] and $\text{Al}_{0.6}\text{Ga}_{0.4}\text{As}$ ($n = 3.2$) [7]. The sizes of these grating mirrors were $12 \mu\text{m} \times 12 \mu\text{m}$ and $10 \mu\text{m} \times 10 \mu\text{m}$, respectively. A more sophisticated structure made of tailored ridges on a silicon ($n \approx 3.5$) substrate allowed a one-dimensional grating with a spatial extent of many square

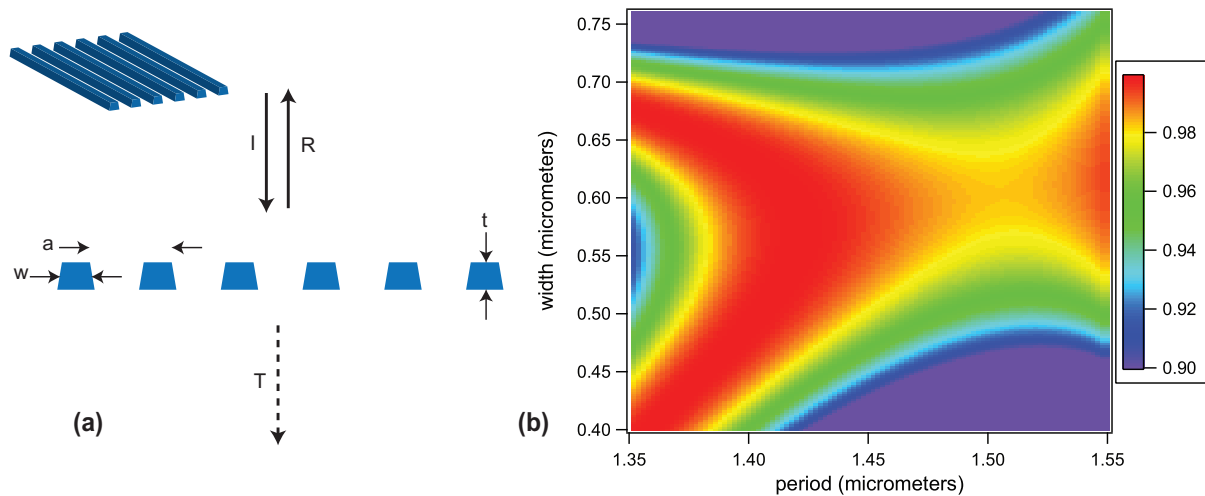


Figure 1. (a) A one-dimensional grating comprised of a periodic array of segments of trapezoidal cross-section, with thickness t , mean finger width w , and period a . The difference between the finger width at the bottom and at the top is $w_{\text{bottom}} - w_{\text{top}} = 160$ nm. Each segment is a dielectric with index of refraction n ; everywhere else is vacuum. With appropriate design, the transmitted beam can be made very small, so that the grating functions as a mirror of near-unity reflectivity. (b) Reflectivity at wavelength $\lambda = 1560$ nm for such a grating with thickness $t = 470$ nm and index of refraction $n = 2.1 + 1.5 \times 10^{-4} i$, calculated with RCWA.

millimeters to be demonstrated [19], owing to the rigidity of the substrate. Two-dimensional gratings consisting of a square array of circular holes have been demonstrated in silicon [20] and InP [8]. A high index contrast allows a broader reflection bandwidth [17], but gratings with a much lower index contrast (3.45:3.17) have been demonstrated [13].

In this work, we consider a one-dimensional grating comprised of a periodic array of dielectric ‘fingers’ with index of refraction $n \approx 2.2$ appropriate to SiN, each finger having a trapezoidal shape with mean width w and thickness t , as illustrated in figure 1(a). The trapezoidal shape is motivated by study of devices we have fabricated, as will be discussed in more detail in section 3.1. The widths at the bottom and top of each finger are taken to be $w_{\text{bottom}} = w + 80$ nm and $w_{\text{top}} = w - 80$ nm, on the basis of measured samples. The periodicity a is chosen to be smaller than the wavelength of the light to be used, $\lambda = 1560$ nm. In between the fingers is vacuum, as are the half-spaces above and below the grating. For a given index of refraction n , the parameters a , w , and t can all be varied in order to tailor the reflectivity. Clearly the idealized structure cannot be completely realized, as the size of the structure will be finite, and fabrication defects will limit the periodicity of the structure. Nevertheless, this structure is amenable to calculation, and provides the starting point for our mirror design.

2.1. Infinite size grating; plane-wave illumination

Calculation of the diffraction pattern for the structure shown in figure 1(a) under plane-wave illumination can be accomplished by means of rigorous coupled-wave analysis (RCWA) [21]. RCWA is a frequency-domain technique in which the total electromagnetic field is expressed

as a countable superposition of plane waves in the regions inside and outside a grating, related by boundary conditions. Outside the grating, the field consists of an incident plane wave and a finite number of forward- and backward-scattered diffracted waves. Within the grating, the field is described as an infinite number of forward- and backward-traveling plane waves with wave vectors given by Floquet theory. When the expressions for the plane waves are coupled by applying Maxwell's equations at the interfaces, the resulting set of equations is reduced to an eigenvalue problem for which user-friendly code has been written [22]. A color plot of the reflectivity of such a structure, as a function of period and finger width, is shown in figure 1(b). We have taken $\lambda = 1560$ nm, $t = 470$ nm, and $n = 2.18 + 1.5 \times 10^{-4} i$. The polarization of the incident beam is taken to be parallel to the grating fingers, and denoted as TE. The peak reflectivity is $R \approx 0.9988$, and a relatively large region is found in the vicinity of $w = 580$ nm and $a = 1420$ nm where the reflectivity exceeds $R = 0.998$. For incident light polarized orthogonally to the grating fingers (TM), the reflectivity $R < 0.1$ over most of the domain shown in figure 1(b). By contrast, a simple unpatterned dielectric slab ($w \rightarrow a$) with the same index of refraction and thickness exhibits a reflectivity of $R \approx 0.34$.

Curves such as those shown in figure 1(b) can be used to try to find a region of parameter space exhibiting high reflectivity while having relatively low sensitivity to fabrication imperfections. For the case of grating fingers with a rectangular cross section, an analytic solution to the diffraction problem has been derived [17], facilitating study with dimensionless combinations of grating parameters. While we have concentrated on gratings designed for TE illumination, gratings with a high reflectivity for polarization perpendicular to the finger direction (TM) have been demonstrated as well [7, 23]. Alternatively, a two-dimensional grating of holes can be used to construct a device whose reflectivity is independent of polarization [14].

Figure 2(a) illustrates calculations of reflection R , transmission T , and absorption A ($R + T + A = 1$) for two gratings we have fabricated with parameters in the high-reflectivity zone of figure 1(b), as a function of wavelength. The thickness is $t = 470$ nm, the period is $a = 1425$ nm, and the average finger widths are $w = 620$ nm (solid curves) and $w = 660$ nm (dashed curves). Ultimately, we are interested in using the gratings as end-mirrors in a Fabry–Perot cavity, so recalling that the finesse of a low-loss Fabry–Perot cavity can be expressed as

$$F = \frac{2\pi}{(1 - R_1) + (1 - R_2)}, \quad (1)$$

where R_1 and R_2 are the reflectivities of the cavity mirrors, figure 2(a) shows $(1 - R)$ rather than R . Clearly it is absorption that ultimately limits the reflectivity at all wavelengths. At $\lambda = 1550$ nm, the grating with $w = 620$ nm is far from absorption-limited, and $T \gg A$. The grating with $w = 660$ nm exhibits a substantially higher reflection at $\lambda = 1550$ nm, but in this case $T \approx 2A$. It is also interesting to note that the absorption of the gratings, $A \approx 1.2 \times 10^{-3}$, is approximately twice that of an unpatterned dielectric slab with the same thickness, $A_{\text{slab}} = 5.3 \times 10^{-4}$. In all cases the polarization of the incident light has been taken parallel to the grating fingers; the reflectivity for the orthogonal polarization varies monotonically from approximately $R = 0.03$ to 0.4 over the range of wavelengths shown.

The discussion has until now assumed an index of refraction with imaginary part $\text{Im}(n) = 1.5 \times 10^{-4}$, taken from a measurement using a low-stress SiN membrane at $\lambda = 1064$ nm [24]. The limiting finesse achievable, in which all cavity losses are set by grating absorption, is $2\pi/A = 5200$. At $\lambda = 1550$ nm it is likely that the absorption is somewhat lower, as the photon energy is further below the SiN bandgap. Indeed, interferometric measurements [25]

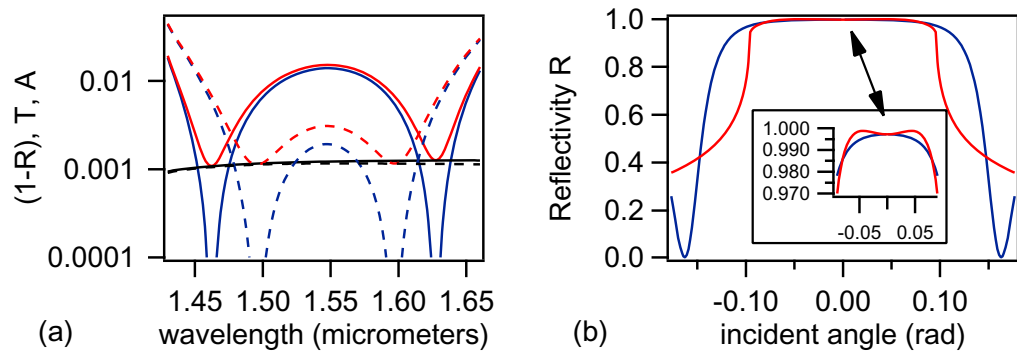


Figure 2. (a) Calculated reflection (expressed as $(1 - R)$) (red), transmission T (blue), and absorption A (black) versus wavelength for two of the gratings we have fabricated. The grating thickness is 470 nm, the period is $w = 1425$ nm, and the solid (dashed) curves refer to gratings with a mean finger width of $w = 620$ nm ($w = 660$ nm). It is noteworthy that, while the reflection and transmission of the two gratings differ substantially from each other and vary strongly with wavelength, the absorption is nearly constant (1.2×10^{-3}) and the same in the two cases. The index of refraction is taken to have imaginary part $\text{Im}(n) = 1.5 \times 10^{-4}$. The absorption of an unpatterned dielectric slab with the same thickness is $A = 5.3 \times 10^{-4}$. (b) Reflectivity as a function of incident angle for the grating with $w = 620$ nm at $\lambda = 1550$ nm; the red (blue) curve corresponds to rotations about an axis parallel (perpendicular) to the grating fingers. The inset shows the reflectivity over the range of -0.09 to 0.09 rad.

of the Brownian motion of a silicon cantilever using light with a wavelength of $\lambda = 1310$ nm showed substantially more heating than measurements made with $\lambda = 1550$ nm, despite the fact that both wavelengths are below the silicon bandgap. An RCWA calculation made with $\text{Im}(n) = 6 \times 10^{-6}$, appropriate to stoichiometric SiN [3], yields a result similar in appearance to that of figure 1(b), but characterized by a peak reflectivity of $R \approx 0.99995$. The corresponding absorption-limited finesse is $F = 125\,000$.

2.2. Confined optical mode

The RCWA calculation assumes plane-wave illumination, and it is of interest to consider how the result would be modified for a confined beam such as is encountered in a Fabry–Perot cavity. While more sophisticated treatments are possible, it is instructive to simply examine the angular dependence of the reflection in the plane-wave case, and compare it to a characteristic diffraction angle for a confined beam. Figure 2(b) shows the reflectivity as a function of incident angle for one of the gratings of figure 2(a) at a wavelength of $\lambda = 1560$ nm. The two curves correspond to rotations around an axis parallel (red) and perpendicular (blue) to the grating fingers. The reflectivity starts to plummet for incident angles larger than $\theta = 0.095$ rad, but it is perhaps more illuminating to note (inset to figure 2(b)) that for rotation angles of $\theta = 0.05$ rad about an axis perpendicular to the grating fingers, the quantity $(1 - R)$ doubles from the value at $\theta = 0$. The far-field diffraction (half-)angle of a Gaussian beam is $\theta = \tan^{-1}(\lambda/(\pi\omega_0))$, where ω_0 is the spot size at the beam waist [26]. Taking $\theta = 0.05$ rad, one finds a corresponding characteristic waist

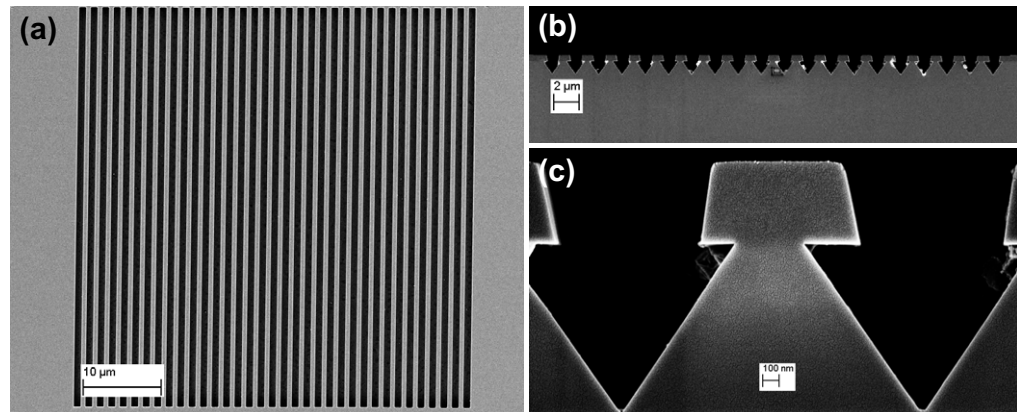


Figure 3. (a) Top view of a grating pattern. (b) Side view of a test sample. The top layer, SiN, is etched with CHF_3 plasma to create finger patterns. (c) Higher magnification image of the sample in (b). The finger patterns are partially undercut with a KOH etch of the underlying silicon. The granular structure on the surface is due to the metal deposited on the surface to avoid charging during SEM imaging.

size of $\omega_0 \approx 10 \mu\text{m}$ at $\lambda = 1560 \text{ nm}$. Thus, a cavity whose finesse is limited by the reflectivity of the grating mirror could be expected to attain its maximum possible finesse only for waist sizes appreciably exceeding $\omega_0 \approx 10 \mu\text{m}$.

3. Experiment

3.1. Device fabrication

The membrane used in this work has dimensions of $1.2 \text{ mm} \times 1.2 \text{ mm} \times 470 \text{ nm}$. It is patterned with 81 different gratings, with various periods and finger widths appropriate to the high-reflectivity zone of figure 1. The fabrication procedure is as follows: silicon (100) wafers are cleaned by a standard procedure to remove organic and ionic contaminants, and immediately transferred to a low-pressure chemical vapor deposition (LPCVD) furnace. In LPCVD, SiN is deposited using a recipe that produces silicon-rich, low-stress SiN. The stress is measured to be $190 \pm 35 \text{ MPa}$, using a commercial film stress measurement system. After deposition, both surfaces of the wafer are spin-coated with photoresist and membrane patterns are defined on the back surface by photolithography. The membrane patterns are then transferred to the SiN by CHF_3 plasma with a reactive ion etch (RIE). The photoresist on both surfaces is stripped off, and the silicon that has been exposed by the RIE process is etched in a KOH solution. The KOH etch stops when it reaches the SiN on the front side of the wafer, creating membranes. After the KOH etch, the wafer with the membranes is briefly dipped in HCl solution, rinsed with deionized water, dried, spin-coated with e-beam resist and diced. E-beam lithography is then used to define the grating structure in the resist and a second RIE step, with the same parameters as the first, is used to transfer the grating pattern to the underlying membrane. Finally, the e-beam resist is stripped away, and the sample is dried in a critical-point drier.

Figure 3 shows test samples made to study various steps in the fabrication procedure. Figure 3(a) shows a top view, with a period of $a = 1500 \text{ nm}$, finger width of $w = 600 \text{ nm}$,

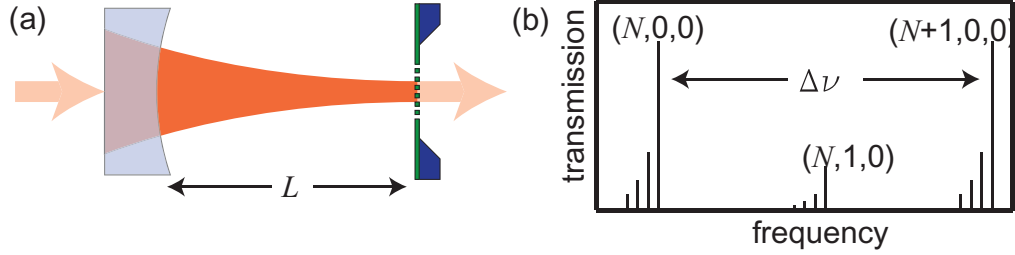


Figure 4. (a) Prototype platform for cavity optomechanics: a Fabry–Perot cavity is formed from a static curved mirror and a mechanically compliant flat mirror. In this case, the mechanically compliant mirror is a sub-wavelength grating patterned in a SiN membrane. (b) Spectrum of plano-concave cavity with length L close to the edge of the stability region defined by the radius of curvature \tilde{R} of the curved mirror. High-order transverse modes are located slightly to the low-frequency side of the fundamental modes, and approximately halfway between adjacent fundamental modes. The mode $\nu_{N,1,0}$ is not located exactly midway between modes $\nu_{N,0,0}$ and $\nu_{N+1,0,0}$.

and lateral dimensions $50\ \mu\text{m} \times 50\ \mu\text{m}$. Occasionally, grating fingers stick to each other in the critical-point drier, and for this reason all of the gratings on our membrane are limited to $50\ \mu\text{m} \times 50\ \mu\text{m}$. The ridges at the top of figure 3(b) are cross-sections of SiN beams defined by RIE, sitting atop a silicon substrate. Figure 3(c) shows triangular profiles in the silicon created by the anisotropic KOH etch used to free the SiN beams from the substrate, and clearly reveals the trapezoidal cross-section of the beams created by the RIE. The top of each beam is typically 160 nm smaller than the bottom. Such trapezoidally-shaped fingers have been found in similar work in different material systems as well [23].

3.2. Cavity

The prototypical platform for cavity optomechanics is shown in figure 4(a). It consists of a Fabry–Perot cavity comprised of a mechanically compliant, nominally flat mirror (right), separated by a distance L from a concave mirror (left) with radius of curvature \tilde{R} . In our case, the mechanically compliant mirror is one of the $50\ \mu\text{m} \times 50\ \mu\text{m}$ sub-wavelength gratings just described. For $L < \tilde{R}$, such a cavity supports stable optical modes whose characteristics are easily related to the cavity geometry as long as the transverse size of the mirrors is sufficiently large [26]. The mode waist is located on the flat mirror, with a spot size ω_0 that becomes very small near the stability boundaries of the cavity, $L \rightarrow 0$ and $L \rightarrow \tilde{R}$. We shall be concerned with cavity lengths $L = \tilde{R}(1 - \epsilon)$, where $\epsilon \ll 1$, in order to have a spot size smaller than the grating mirror and a free spectral range $\Delta\nu = c/(2L)$ commensurate with the scanning range of our laser. For such a geometry, it may be shown that the waist size ω_0 and the spot size on the curved mirror ω_1 are given by

$$\omega_0 = \sqrt{\frac{\lambda \tilde{R}}{\pi}} \epsilon^{1/4}, \quad \omega_1 = \sqrt{\frac{\lambda \tilde{R}}{\pi}} \epsilon^{-1/4}. \quad (2)$$

If the spot sizes ω_0 and ω_1 are not substantially smaller than the size of the mirrors, then these equations are not valid and a numerical analysis is required [26, 27].

For a cavity with a plano-concave geometry such as illustrated in figure 4(a), the cavity resonance frequencies are given by

$$\nu_{N,m,n} = \Delta\nu \left[N + \frac{m+n+1}{2} \left(1 - \frac{1}{\pi} \sqrt{\epsilon} \right) \right]. \quad (3)$$

Here the integer N labels the longitudinal modes, and integers $m \geq 0$ and $n \geq 0$ label transverse modes. The modes with transverse mode indices such that $m+n$ is even are located near the fundamental modes ($m=n=0$), and spaced by $\delta\nu = \Delta\nu \sqrt{\epsilon}/\pi$. The modes with $m+n$ odd are located between the fundamental modes, and also spaced by $\delta\nu$. This mode structure is shown in figure 4(b).

We have implemented such a cavity in a small vacuum chamber maintained at a pressure of 1.3×10^{-5} Pa (1.3×10^{-7} mbar) with an ion pump. All of the results to be discussed here employ a grating with period $a = 1410$ nm and finger width $w = 620$ nm. The cavity length L can be varied with a stick/slip actuator with a resolution of 30 nm. The curved mirror is characterized by a radius of curvature $\tilde{R} = 25$ mm and diameter of $\phi = 7.75$ mm. It has a dielectric coating with a reflectivity given by $1 - R = 1.6 \times 10^{-4} \pm 2 \times 10^{-5}$ at $\lambda = 1560$ nm. In order to limit losses at the curved mirror, we envision a cavity in which the length L is sufficiently far from the stability boundary that the spot size of the confined mode on the curved mirror is no greater than approximately half the radius, or $\omega_1 = 1.5$ mm. Using (2), this implies $\epsilon \tilde{R} > 790$ nm, corresponding to a waist size of $\omega_0 > 8.3$ μ m.

Light is coupled into the cavity by means of the apparatus shown in figure 5. A tunable ‘probe’ laser is passed through a Faraday isolator and mode-matched into the cavity by means of two lenses. The (linear) polarization of the light entering the cavity can be rotated by means of a half-wave plate, in order to align the polarization relative to the grating orientation. An electro-optic modulator (EOM) can be used to phase-modulate the laser so as to generate sidebands to probe the cavity modes shown in figure 4(b), as discussed in section 4.2, or to derive a Pound–Drever–Hall (PDH) error signal. The beam reflected by the cavity is spatially separated from the ingoing beam by means of the Faraday isolator. Light transmitted by the cavity exits the vacuum chamber and can be monitored with both a photodiode and a camera.

4. Optical characterization

4.1. Transmission, reflection, finesse

Figure 6(a) shows the cavity transmission and reflection curves in the vicinity of a resonance at our target wavelength of $\lambda = 1560$ nm. The curves were made by sweeping a tunable laser (linewidth < 100 kHz) by means of a piezoelectric actuator. The laser frequency is swept over a time of 1 ms, and the frequency axis is calibrated by adding sidebands (not shown) to the laser, at a frequency of 28 MHz. The transmission peaks of the carrier and sidebands are all fit to Lorentzians, a process that is repeated 20 times. The transmission peak has a full-width at half-maximum of 3.03 ± 0.08 MHz, corresponding to a finesse of $F = 1980 \pm 50$. The uncertainty is dominated by the standard deviation (type A evaluation) of the 20 measurements. From (1) we can then infer $(1 - R_2) = 3.0 \times 10^{-3} \pm 8 \times 10^{-5}$.

The primary transmission peak visible in figure 6(a) is that of a TEM₀₀ mode. In addition, a small, much broader peak is visible at a frequency 30 MHz higher. This peak is caused by excitation of a higher-order mode due to imperfect mode matching. In the optomechanical cooling to be described in section 5.2, light injected into the cavity is tuned to well within one

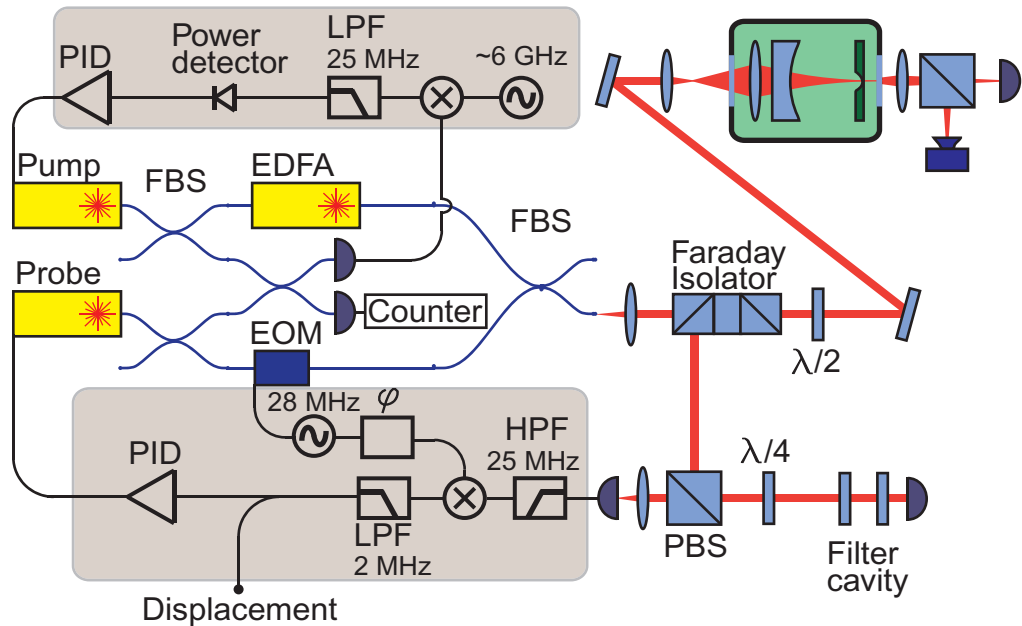


Figure 5. Experimental setup. A ‘probe’ laser is phase-modulated at 28 MHz by means of an EOM and sent into a Faraday isolator. The (linear) polarization of the emerging beam can be adjusted by means of a $\lambda/2$ plate, and the beam is mode-matched into the cavity with two lenses. The beam reflected by the cavity is spatially separated from the ingoing beam by means of the Faraday isolator, and the reflected signal is detected, high-pass filtered (HPF), and demodulated at 28 MHz to derive a PDH error signal. The error signal is used to maintain the probe laser resonant with the cavity at low frequencies ($f < 12$ kHz), and to infer the membrane displacement at frequencies ($f > 12$ kHz) outside the servo bandwidth. A second ‘pump’ laser, amplified with an erbium-doped fiber amplifier (EDFA), can be combined with the probe laser by means of a fiber beamsplitter (FBS) and simultaneously injected into the cavity. It is beat against the probe laser, and offset-locked to a frequency $\Delta\nu' \approx 6$ GHz relative to the probe. When the pump is in use, a low-finesse filter cavity with a free spectral range of 12 GHz is used to minimize unwanted reflected pump light in the displacement detection signal.

cavity linewidth of the TEM_{00} mode, and the radiation pressure associated with higher-order modes such as this one is negligible.

Figure 6(b) shows the cavity finesse as a function of wavelength over a range of $\lambda = 1500\text{--}1608$ nm. At each wavelength, the error bars correspond to the standard deviation of 20 measurements. The highest finesse we measure is $F = 2830 \pm 60$ at $\lambda = 1509$ nm, corresponding to $(1 - R) = 2.06 \times 10^{-3} \pm 5 \times 10^{-5}$. Between $\lambda = 1527$ and 1560 nm the finesse plummets to a minimum value of $F = 107 \pm 8$. We believe this is a consequence of resonant optical coupling to high order transverse modes with high losses, rather than an actual diminution of the grating reflectivity in this wavelength interval. This loss mechanism has been observed before [28], and is exacerbated by working near the critical point of a cavity with a small mirror. Not only does the mode density increase when the critical point is approached, as

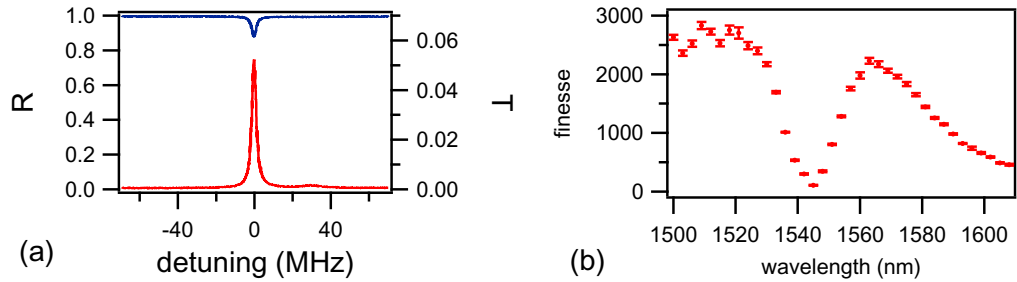


Figure 6. (a) Transmission peak (red) and reflection dip (blue) at $\lambda = 1560$ nm for a cavity using a grating with period $a = 1410$ nm and mean finger width $w = 620$ nm as the output coupler. The main transmission peak is that of the TEM_{00} mode; the small peak observed at a frequency 30 MHz higher reflects excitation of a higher-order mode due to imperfect mode matching. (b) Finesse versus wavelength for the same grating. While the reduction in finesse above $\lambda = 1565$ nm is presumably due to lower grating reflectivity, we believe that the drop between $\lambda = 1527$ and 1560 nm is a consequence of resonant optical coupling to high order transverse modes with high losses.

shown in (3), but the losses of the higher-order modes increase due to their greater spatial extent relative to the small mirror. It is notable that the scatter in the measured finesse for wavelengths in the vicinity of $\lambda = 1500$ –1530 nm is far greater than the measurement uncertainty associated with each point. We believe that these (repeatable) fluctuations are also due to resonant optical coupling to high order transverse modes.

4.2. Spatial mode size

We now address how the finesse depends on the cavity length, and correspondingly the geometry of the confined optical mode. The subject of diffraction losses in cavities with very small mirrors, as encountered in optomechanics, has recently been addressed [27]. In the present work, an additional loss mechanism arises for a grating of small spatial extent, which is the angular dependence of the reflectivity of the grating. As we will show, the optimum finesse we are able to achieve seems to be limited by both diffraction losses and the angular response of the grating.

In order to accurately measure the cavity length L , we first use an EOM to generate sidebands on the laser frequency ν_1 with frequencies $\nu_1 \pm \nu_{\text{rf}}$, where $\nu_{\text{rf}} \simeq 3$ GHz is generated by a synthesizer. The free spectral range of our cavity is $\Delta\nu = c/(2L) \approx 6$ GHz. We sweep the laser frequency ν_1 and adjust ν_{rf} so that the sidebands probe adjacent fundamental resonances simultaneously, at which point $\nu_{\text{rf}} = \Delta\nu/2$ and $L = c/(4\nu_{\text{rf}})$. The mode $\nu_{N,1,0}$ is not located exactly midway between modes $\nu_{N,0,0}$ and $\nu_{N+1,0,0}$, and thus is not resonant with the carrier. A plot of the finesse as a function of cavity length at $\lambda = 1560$ nm is shown in figure 7(a). The dominant contribution to the error bars is the uncertainty (type B evaluation) in adjusting ν_{rf} to the exact centers of the cavity resonances. The finesse increases and reaches a maximum with increasing cavity length, and then diminishes as the cavity is brought to the stability boundary. Qualitatively, we can understand this, as the size of the TEM_{00} mode waist diminishes when $L \rightarrow \tilde{R}$, reducing the losses due to the limited spatial extent of the grating mirror. If the waist

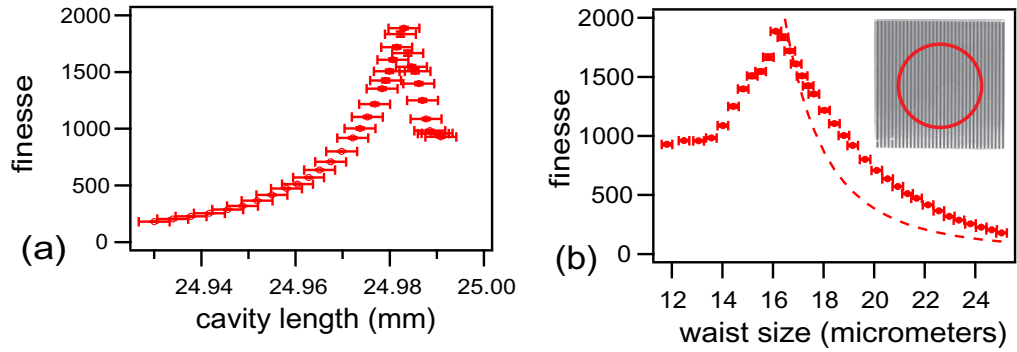


Figure 7. (a) Finesse versus cavity length at $\lambda = 1560$ nm. (b) Finesse versus waist size corresponding to cavity length in (a). The dotted line is the prediction of a crude model in which the finesse is set solely by losses beyond the edge of a perfect ($R = 1$) square mirror with side $d = 50$ μm . The inset shows the grating, along with a circle with a radius equal to the spot size ω_0 that maximizes the finesse. The circle contains about 23 grating fingers.

size is made too small, however, the grating reflectivity drops as discussed in section 2.2; in addition, power may be lost at the curved mirror if the spot size ω_1 is no longer small compared to its diameter.

In order to be more quantitative, we use (2) relating the spot sizes on the curved mirror and the grating to the distance $\tilde{R} - L$ between the cavity length L and the stability boundary \tilde{R} . Unfortunately, the radius of curvature \tilde{R} is not known well enough in advance to allow a useful inference of $\tilde{R} - L$ from the length measurements shown in figure 7(a). In order to determine $\tilde{R} - L$, we employ a spectroscopic measurement of the higher-order transverse modes of the cavity. We phase-modulate the laser at ν_{rf} and sweep the carrier ν_1 about the mode $\nu_{N,1,0}$ (figure 4(b)), and adjust ν_{rf} so that the lower sideband is resonant with the fundamental resonance $\nu_{N,0,0}$ at the same time that ν_1 is resonant with the mode $\nu_{N,1,0}$. At this point, $\nu_{\text{rf}} = \Delta\nu/2 - \Delta\nu\sqrt{\epsilon}/(2\pi)$, and ϵ can be readily inferred since $\Delta\nu$ is known. It is worth noting that (2) relating the spot size ω_0 to ϵ is strictly valid only in the limit that the mirror size is very large compared to the spot size, while our grating mirror is only $d = 50$ μm on a side.

Figure 7(b) shows the finesse as a function of the spot size on the grating, where the spot size has been determined by use of (2). The error bars reflect only measurement uncertainties; the actual waist size becomes less and less certain as it increases towards the size of the grating mirror, since (2) becomes less and less valid. Subject to this caution, the finesse peaks for an inferred waist size of $\omega_0 \approx 16$ μm , at which point the spot size on the curved mirror is $\omega_1 = 770$ μm , well below the mirror radius. It is apparent that the peak finesse is limited not by the curved mirror, but rather by a compromise between losses beyond the edge of the grating and the loss of grating reflectivity with angle associated with spatial components comprising beams with a waist below $\omega_0 = 16$ μm . The inset to figure 7(b) shows a circle with a radius equal to $\omega_0 \approx 16$ μm superposed upon the grating.

Indeed, we saw in section 2.2 that a plane wave incident on a grating such as ours at an angle θ corresponding to a waist size of $\omega_0 \approx 10$ μm would experience a value of $(1 - R)$ twice that at normal incidence. The fact that the measured finesse drops to approximately half its peak value when the waist is reduced to a size of $\omega_0 \approx 10$ μm is highly suggestive that

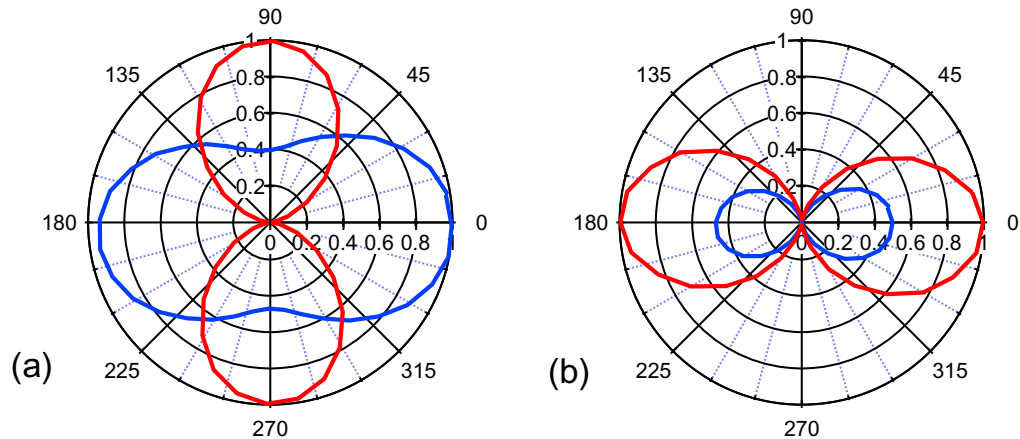


Figure 8. (a) Polar plot r, θ of power (r) transmitted through a polarizer oriented along an axis described by polar angle θ relative to the horizontal. The red curve describes the light incident on the cavity, which is linearly polarized in the vertical direction, parallel to the grating fingers. The blue curve describes the cavity transmission on resonance, normalized to its peak value. The output light is elliptically polarized, with its principal axis nearly horizontal. (b) Same, but the incident light is polarized in the horizontal direction, perpendicular to the grating fingers. The finesse is very low in this case, and the polarization of the transmitted light remains horizontal. The scale of the transmitted power has been normalized to half the peak value for clarity.

the dependence of the grating reflectivity on angle is the reason. One can estimate the loss in finesse as the waist size increases by means of a crude model, in which the intensity distribution at the waist is taken to be Gaussian with spot size ω_0 , the flat mirror is taken to be a square of side d with perfect reflectivity $R = 1$, and the space outside the mirror is taken to have reflectivity $R' = 0.34$, corresponding to unpatterned SiN. The curved mirror is also taken to have infinite spatial extent and perfect reflectivity, so that all optical losses occur where the Gaussian beam spills over the edge of the small square mirror. The optical losses are then given by $\kappa = (1 - R')(1 - \text{erf}^2(d/(\sqrt{2}\omega_0)))$, and the corresponding finesse $F = 2\pi/\kappa$ is shown in the dotted line in figure 7(b). It is notable that the observed finesse exceeds the predictions of this crude model for all waist sizes above $\omega_0 \approx 17 \mu\text{m}$, consistent with the fact that the actual spatial modes of a cavity with small mirrors deviate from the modes of infinite-size mirrors by adopting a shape that gives a lower round-trip diffraction loss [27]. The fact that the finesse reaches a sharp peak, rather than a plateau, suggests that it is currently limited by both of the mechanisms discussed here, and is strong motivation to pursue a grating with a larger area.

4.3. Polarization

Since the one-dimensional grating we employ is highly polarization dependent, as discussed in section 2.1, one might assume that the cavity would function as a linear polarizer. This is in fact not the case, as shown in figure 8, relating the polarization at the output of the cavity to

that at the input. In figure 8(a), the injected light is polarized vertically, parallel to the grating fingers; the exact polarization angle is found by maximizing the peak transmitted power. This is the configuration used for all of the results described to this point. The red curve is a polar plot of the incident power transmitted through a polarizer oriented along an axis described by polar angle θ relative to the horizontal. The blue curve is a similar plot of the power transmitted on resonance (normalized to its maximum power as a function of θ), and it is clear not only that the polarization is elliptical, but that the principal axis of the ellipse has been rotated by 90° relative to the incident polarization.

We interpret this as a consequence of birefringence within the cavity, so that the cavity eigenstates have a small TM component. Therefore, after a large number of round trips inside the cavity, light injected with an initial TE polarization acquires a weak perpendicular polarization component. Because of the large difference in grating reflectivity for the two polarizations, the TM component is much more favorably transmitted. The form of the polar plot in figure 8(a) can be used to infer that the output polarization is an ellipse with its major axis horizontal and eccentricity $\varepsilon \approx 0.75$. The circulating field striking the output coupler then must have an elliptical polarization with a ratio of horizontal to vertical electric field amplitudes of $1/\varepsilon\sqrt{T_{\text{TE}}/T_{\text{TM}}}$, where T_{TE} (T_{TM}) is the (power) transmission of the grating for TE (TM) polarized light. It can then be shown that the power transmitted by the output coupler is

$$\begin{aligned} T_{\text{OC}} &= \left(\frac{\sin^2 \theta}{T_{\text{TE}}} + \frac{\cos^2 \theta}{T_{\text{TM}}} \right)^{-1} \\ &\approx \frac{T_{\text{TE}}}{\sin^2 \theta} \\ &= 2.78 T_{\text{TE}}, \end{aligned} \quad (4)$$

where $\theta = \tan^{-1}\varepsilon = 0.64$, so that the output coupler transmits a factor of 2.78 more light than it would if there were no birefringence. Thus, the birefringence provides a substantial loss mechanism limiting the finesse. Taking the absorption given by RCWA ($A = 1.2 \times 10^{-3}$), the transmission T_{TE} of the grating would have to be $T_{\text{TE}} = 6.5 \times 10^{-4}$ in order to provide the finesse $F = 1980$ that we observe; in the absence of birefringence, the corresponding finesse would be $F = 3100$.

It is not at the moment clear which element is principally responsible for the birefringence. Since the stress in the grating fingers is larger along the length than across the width, as discussed in section 5.1, it is likely that the grating is birefringent. At the same time, stress-induced birefringence is a well-known phenomenon in high reflectivity dielectric mirrors unless special care is taken in mounting them [29], and in fact we have observed birefringence in symmetric cavities made employing dielectric mirrors identical to the curved one used here. An appealing possibility is to apply stress to the dielectric mirror in such a way as to create birefringence with the fast axis aligned parallel to the slow axis of any birefringence present in the grating. If the magnitude of the birefringence in the dielectric were made equal to that in the grating, the two would compensate each other, and the associated loss would be eliminated.

Figure 8(b) shows a similar polar plot for the case that the polarization of the light injected into the cavity is perpendicular to the grating fingers. In this case the blue curve representing the transmitted power has the same functional dependence on θ as does the injected light, showing that the transmitted light has the same linear polarization as that which is injected. The normalization has been adjusted by a factor of two for clarity. Because of the very low reflectivity of the grating in this direction, light injected with TM polarization makes very few

round trips of the cavity and thus does not significantly probe the cavity birefringence, resulting in a polarization state unchanged by the cavity.

5. Mechanical characterization

5.1. Passive mechanical characterization

To probe the mechanical motion of the membrane, we implement the PDH setup shown in figure 5 with a modulation frequency $\nu_{\text{rf}} = 28$ MHz. Feedback is used to maintain the laser, with a power of approximately $150 \mu\text{W}$, resonant with the cavity at frequencies below 12 kHz. The PDH error signal is proportional to the membrane displacement at higher frequencies, where feedback is ineffective.

In order to calibrate the PDH error signal, we sweep the laser frequency ν over a cavity resonance and digitize the PDH signal as a function of time. The sidebands of the error signal, separated from each other by $2\nu_{\text{rf}} = 56$ MHz, allow us to calibrate the temporal axis in terms of optical frequency. The central feature of the PDH signal then has a known slope $dV/d\nu$. In practice, this calibration is compromised by low-frequency fluctuations in the cavity length as the laser is swept. For this reason, we sweep the laser frequency rapidly (but still slowly compared to the cavity decay rate), and average over 20 sweeps. The typical uncertainty in $dV/d\nu$ associated with the standard deviation of the 20 measurements (type A evaluation) is 10%. Small changes in the cavity length dL are then related to small changes in the resonance frequency $d\nu$ by $d\nu/\nu = -dL/L$, from which we obtain the relation between signal voltage and cavity length for fixed laser frequency $dV/dL = -(\nu/L) dV/d\nu$. L and ν are both known with sufficient accuracy that the uncertainty in dV/dL is dominated by the 10% uncertainty in $dV/d\nu$.

The red curve in figure 9(a) shows the mechanical spectrum made with a weak resonant probe as observed on a spectrum analyzer (resolution bandwidth 30 Hz) in the frequency range from 120 kHz to 1.85 MHz. Hundreds of mechanical resonances are present, and although the mode density increases with frequency, the resonances are well-resolved at even the highest frequencies shown.

To frame our discussion of the dynamics, we express the membrane displacement $z(x, y, t)$ as a sum of products of normal modes $g_{mn}(x, y)$ with time-dependent factors $q_{mn}(t)$

$$z(x, y, t) = \sum_{m,n} q_{mn}(t) g_{mn}(x, y). \quad (5)$$

For a uniform square membrane, the mode functions g_{mn} are given by $g_{mn}(x, y) = \sin \frac{m\pi x}{d} \sin \frac{n\pi y}{d}$, where m and n are positive integers, and d is the length of a side of the membrane. In the absence of applied forces, the amplitudes $q_{mn}(t)$ satisfy the differential equation

$$\ddot{q}_{mn} + \Gamma_{mn}^{\text{intr}} \dot{q}_{mn} + \omega_{mn}^2 q_{mn} = \frac{F_{\text{th}}(t)}{m_{\text{eff}}}, \quad (6)$$

where $F_{\text{th}}(t)$ is the thermal Langevin force, whose power spectral density is given by $S_F(\omega) = 4m_{\text{eff}}\Gamma_{mn}^{\text{intr}}k_{\text{B}}T$. The ω_{mn} are the mechanical eigenfrequencies, and m_{eff} is the membrane effective mass. For a uniform square membrane of mass m , the eigenfrequencies are related to each other by $\omega_{mn}^2 = \omega_{11}^2(m^2 + n^2)/2$, and the effective mass $m_{\text{eff}} = m/4$ [30]. $\Gamma_{mn}^{\text{intr}}$ is the intrinsic damping of the mode labeled by (m, n) , related to the mechanical quality factor by $\Gamma_{mn}^{\text{intr}} = \omega_{mn}/Q_{mn}$. In thermal equilibrium at temperature T , the amplitude $q_{mn}(t)$ of each mode

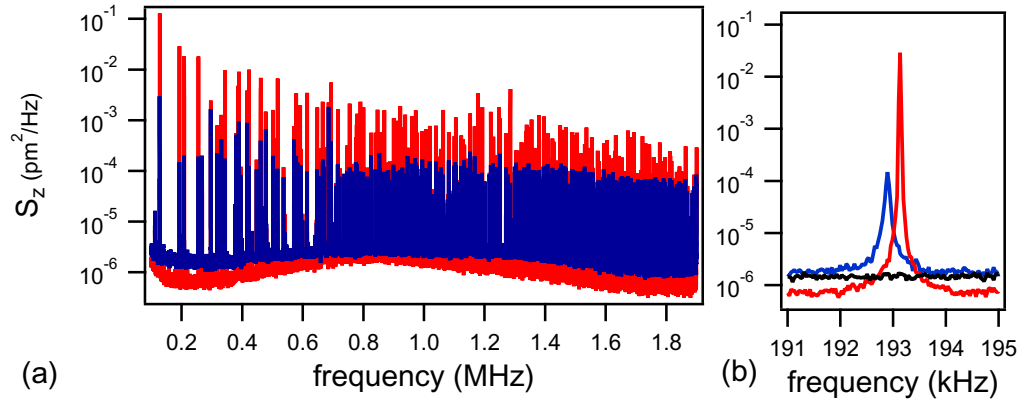


Figure 9. (a) Red curve: spectrum of mean-square membrane displacement at location (x_0, y_0) of optical waist, obtained from PDH signal. Blue curve: an additional laser, detuned by 800 kHz to the red of an adjacent longitudinal mode of the cavity, provides optical cooling of all of the mechanical modes. (b) Expanded view of spectrum of mode labeled by $(m, n) = (1, 2)$. The linewidth is limited by the resolution bandwidth of the spectrum analyzer (30 Hz). Red curve: the noise floor corresponds to a displacement sensitivity of $7 \times 10^{-31} \text{m}^2 \text{Hz}^{-1}$, or $8.4 \times 10^{-16} \text{m} \sqrt{\text{Hz}}^{-1}$. Blue curve: an optically induced frequency shift of 240 Hz accompanies the cooling. Black curve: displacement signal when probe is off-resonance, showing contribution to background from pump laser.

is given by equipartition, and the measured displacement $z(x, y, t)$ is proportional to the mode function $g_{mn}(x, y)$ evaluated at the position of the laser spot.

Returning to figure 9(a), the fundamental mode has a frequency of $\nu_{11} = 128$ kHz, and the next two modes are at frequencies $\nu_{12} = 193$ and $\nu_{21} = 209$ kHz. The ratios of the mode frequencies, $\nu_{12}/\nu_{11} = 1.51$ and $\nu_{21}/\nu_{11} = 1.63$, are split about the ratio $\sqrt{5/2} \approx 1.58$ expected for a uniform square membrane. This is a consequence of the asymmetric stress induced in the membrane by patterning it with gratings; similarly, the mode eigenfunctions $g_{mn}(x, y)$ and effective mass m_{eff} cannot be expected to have exactly the same forms as those for the uniform square case. By fitting the measured frequencies of the ten lowest-frequency modes to the result for a square membrane with different stresses in the \hat{x} and \hat{y} directions, we infer a stress of 158 ± 2 MPa along the grating fingers and 120 ± 2 MPa in the perpendicular direction.

We now focus attention on the mode labeled by $(m, n) = (1, 2)$, which we have determined from measurements of mechanical ringdown [9] to have the highest quality factor, $Q_{12}^{\text{intr}} = 7.5 \times 10^5$, of any mode that we have measured. For a lightly-damped oscillator ($\Gamma_{mn} \ll \omega_{mn}$), the $q_{mn}(t)$ can be expressed as

$$q_{mn}(t) = A_{mn}(t) \cos(\omega_{mn}t - \phi_{mn}(t)) \quad (7)$$

where $A_{mn}(t)$ is a slowly-varying amplitude and $\phi_{mn}(t)$ is a slowly-varying phase. In order to more fully characterize the mechanical excitation, the PDH signal is demodulated at frequency ν_{12} by means of a lockin amplifier, with a bandwidth of 50 Hz. The lockin amplifier gives

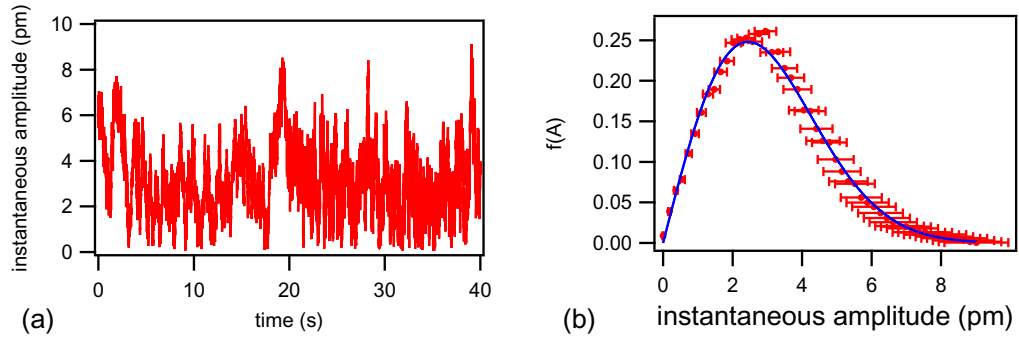


Figure 10. (a) Instantaneous oscillation amplitude $A_{12}(t)$ sampled every 2 ms. $A_{12}(t)$ fluctuates over a range from nearly zero to 9 pm in the observation time of 40 s, with a mean value $\langle A(t) \rangle = 3.2$ pm. (b) Corresponding histogram, together with fit to a distribution derived from Boltzmann statistics. The error bars reflect the 10% uncertainty in the PDH calibration.

the instantaneous amplitude $A_{12}(t) g_{12}(x_0, y_0)$, where (x_0, y_0) is the location of the laser spot. Figure 10(a) shows $A_{12}(t)$ sampled every 2 ms, where $g_{12}(x_0, y_0)$ is taken to be that appropriate to a uniform membrane. It fluctuates over a range from nearly zero to 9 pm in a time of 40 s, with a mean amplitude of $\langle A(t) \rangle = 3.2$ pm and a mean-square amplitude $\langle A^2(t) \rangle = 12.5$ pm².

In the case of thermal equilibrium, Boltzmann statistics predict a distribution of the form

$$f_{mn}(A) = \frac{m_{\text{eff}} \omega_{mn}^2}{k_B T} A e^{-\frac{m_{\text{eff}} \omega_{mn}^2 A^2}{2k_B T}} \quad (8)$$

and a relation between the first and second moments of $\langle A^2 \rangle / \langle A \rangle^2 = 4/\pi \approx 1.27$. The mean and second moment of the data give $\langle A^2 \rangle / \langle A \rangle^2 = 1.26$. A histogram of $A_{12}(t)$ is shown in figure 10(b), in which the error bars reflect the uncertainty in the PDH calibration. Also shown is a fit to $f_{12}(A)$, in which the temperature is the only free parameter. The agreement is very good, and yields a temperature of 342 ± 4 K, where the uncertainty in the fit parameter does not include a contribution from the error bars. Indeed, fitting to the lower or upper extremities of the error bars yields a fit that is much less satisfactory, suggesting that our estimate of the uncertainty in the PDH calibration is on the high side. The fact that the extracted temperature is greater than the ambient temperature is not completely understood. It is important to note that equations concerning thermal equilibrium involve properties of the membrane, in addition to the measured oscillation amplitude. Thus, the effective mass in (8) is taken to be one-fourth of the physical mass of the patterned membrane, $m_{\text{eff}} = 5.36 \times 10^{-10}$ kg, and the eigenmodes $g(x, y)$ relating the measured displacement $z(x, y, t)$ to the mode antinode amplitude $A(t)$ are taken to be those of an unpatterned membrane. Both of these choices are approximations, as we have not attempted an exact numerical solution, and may contribute to the discrepancy from room temperature. It may also be the case that excess technical noise is present atop the fundamental thermal noise, or that a very small blue detuning of the probe laser contributes a weak optical antidamping force. It is notable that if we infer the temperature only from the mean-square amplitude, rather than the full statistical distribution, we find $T = 354 \pm 71$ K, where the (much larger) uncertainty arises from the PDH displacement calibration.

5.2. Optical cooling

The effect of radiation pressure is to add a generalized force $F_{mn}(t)$ [30] to the Langevin force in (6). In the case that the applied force is the radiation pressure associated with a Gaussian optical mode with spot size ω_0 centered at position (x_0, y_0) on the membrane, the generalized force $F_{mn}(t)$ is given by

$$F_{mn}(t) = F^{\text{RP}}(t) e^{-\pi^2 \omega_0^2 (m^2 + n^2) / (8d^2)} \phi_{mn}(x_0, y_0), \quad (9)$$

where $F^{\text{RP}}(t)$ is the total applied radiation pressure force. In our case, $\omega_0 \ll d$, and to very good approximation $F_{mn}(t) \approx F^{\text{RP}}(t) \phi_{mn}(x_0, y_0)$ for the low-order mechanical modes. For a high- Q mechanical oscillator, the radiation pressure is correlated with the mechanical motion, with the well-known consequence that the damping rate in (6) is modified. The new damping rate is given by $\Gamma^{\text{intr}} \rightarrow \Gamma^{\text{intr}} + \Gamma^{\text{RP}}$, where Γ^{RP} is proportional to the cooling laser power, and may be positive or negative depending on the sign of the detuning [1]. It can then be shown from (6) that the mean-square displacement is equivalent to that given by equipartition

$$\langle q_{mn}^2 \rangle = \frac{k_B T_{\text{eff}}}{m_{\text{eff}} \omega_{mn}^2}, \quad (10)$$

but at an effective temperature $T_{\text{eff}} = T (\Gamma^{\text{intr}} / (\Gamma^{\text{intr}} + \Gamma^{\text{RP}}))$.

To implement optical cooling, the cooling ('pump') laser shown in figure 5 is combined with the probe laser by means of a fiber beamsplitter and simultaneously injected into the cavity. The probe laser power is set to approximately 200 μW for these experiments. In order that the reflection of the pump not perturb the displacement measurement, it is tuned near to an adjacent longitudinal mode, separated by 6 GHz, and a low-finesse filter cavity is used to separate the pump and probe beams. As shown in figure 5, the pump is beat against the probe laser, and offset-locked to a frequency $\Delta\nu' \approx 6$ GHz relative to the probe. The exact offset frequency can be set by means of a synthesizer to allow precise control of the detuning of the cooling laser. The filter cavity is comprised of two flat glass plates, each coated with a reflectivity of $R \approx 0.7$, and has a free spectral range of 12 GHz. The length of the cavity is set by means of a piezoelectric actuator to be resonant with pump light, so that the cavity reflection is minimized for the pump and maximized for the probe. No active stabilization of this cavity is required.

The blue curve in figure 9(a) shows the mechanical spectrum in the presence of the cooling laser, detuned to the red of a cavity mode by 800 kHz, or approximately one-fourth of the cavity linewidth $\Delta\nu/F$. This is near the optimal detuning $(1/(2\sqrt{5}))\Delta\nu/F$ for cooling in the limit of low mechanical frequency (far from sideband-resolved). The mean-square amplitude of most of the modes drops by over an order of magnitude. The modes are not cooled equally, a consequence of their different couplings $g_{mn}(x_0, y_0)$ to the radiation pressure, different frequencies, and different mechanical quality factors. The black trace in figure 9(b) shows the displacement signal resulting when both the pump and probe lasers are present, but off resonance. The background level rises, a consequence of amplitude noise from the cooling laser (not completely removed by the filter cavity) entering the detection system. An optically-induced frequency shift is clearly seen in figure 9(b) as well.

Figure 11(a) shows mechanical spectra made with a spectrum analyzer (resolution bandwidth 1 Hz) for a series of cooling laser powers. As the cooling laser power is increased, the mechanical spectra diminish in amplitude, broaden, and experience a frequency shift. The effective temperatures, inferred by integrating the power spectral densities in figure 11(a) to obtain $\langle q_{12}^2 \rangle$ and then using (10), are shown as a function of cooling laser power in

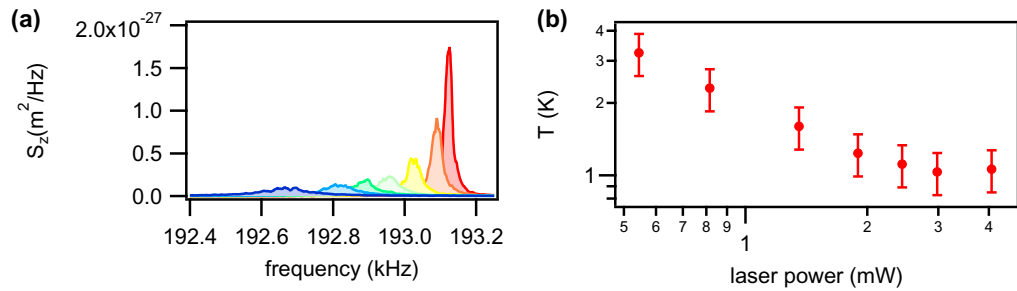


Figure 11. (a) Power spectral densities of the displacement at an antinode of the mode labeled by $(m, n) = (1, 2)$, taken from a spectrum analyzer, for a series of cooling laser powers. (b) Effective temperature of the $(1, 2)$ mode based on integrating the power spectra shown at the left to obtain the mean-square displacement.

figure 11(b). For small cooling laser powers, the width of the measured mechanical spectrum is limited by the resolution bandwidth of the spectrum analyzer, and for this reason points corresponding to effective temperatures above 3 K are not shown. For higher laser powers, the effective temperature drops inversely proportional to power, as expected, until it flattens out at $T_{\text{eff}} = 1 \pm 0.2$ K. Here the uncertainty is primarily due to the determination of the slope of the PDH signal relating signal voltage to mechanical displacement. Alternatively, the mean-square displacement of the antinode is reduced by a factor of 313 by optical cooling, which depends on neither the membrane effective mass m_{eff} nor the PDH calibration. It is not clear at the moment why the cooling saturates. One possibility is local heating caused by material absorption as the circulating optical power increases; it is also possible that pump laser noise is not adequately removed by the low-finesse filter cavity as the power is increased. The issue is currently under investigation.

6. Conclusion and outlook

We have demonstrated sub-wavelength gratings in SiN to be a viable platform for optomechanics. Using a grating etched from a SiN membrane as the end mirror of a Fabry–Perot cavity, we demonstrated a cavity finesse of $F = 1980$ at the target wavelength of $\lambda = 1560$ nm, and a finesse of $F = 2830$ at $\lambda = 1509$ nm. The latter figure corresponds to a grating reflectivity of $R = 1 - 2.06 \times 10^{-3}$. RCWA calculations, assuming an absorption characterized by $\text{Im}(n) = 1.5 \times 10^{-4}$, imply $R < 1 - 1.2 \times 10^{-3}$, which suggests that we are not more than a factor of two away from the limitation imposed by material absorption. We have identified a number of mechanisms, in addition to absorption and scattering from fabrication defects, contributing to the optical losses. The reduction in grating reflectivity as the spot size is reduced would be immediately improved by use of a larger grating, as would the optical coupling to lossy high-order optical modes which can accompany working near the critical point of the Fabry–Perot cavity. Cavity birefringence is another mechanism providing substantial loss, apparently limiting the finesse at $\lambda = 1560$ nm from a potential $F \approx 3000$ to 2000. This loss mechanism may be overcome if we are able to compensate birefringence in the membrane by appropriate stress of the dielectric mirror.

We are currently working to overcome these loss mechanisms. While the yield of our $50\ \mu\text{m} \times 50\ \mu\text{m}$ grating structures is nearly 100%, we have already fabricated gratings with a $75\ \mu\text{m} \times 75\ \mu\text{m}$ size with yield better than 50%. There are other approaches to obtaining a larger grating as well, including employing a structure with a substrate, making a two-dimensional grating, and the use of a dry technique to remove the e-beam resist in the final step. The two-dimensional grating is of particular interest since it can be made polarization-insensitive and should not exhibit birefringence. Finally, we are investigating the use of stoichiometric SiN, which would give an absorption-limited finesse more than an order of magnitude higher.

We have shown that the mechanical motion of the membrane is well-described by normal modes whose slowly-varying amplitudes are characterized by a Boltzmann distribution, and we are able to optically cool one of the modes, at a frequency of 193 kHz, to $T_{\text{eff}} \approx 1\ \text{K}$ from room temperature. The current membrane is not particularly well adapted to cooling, as it was made very large in order to accommodate 81 gratings. We are currently fabricating smaller membranes with fewer gratings. A membrane $120\ \mu\text{m}$ on a side would have a mass one hundred times smaller than the one described here, and the fundamental frequency of 1.3 MHz would bring it nearly into the resolved-sideband regime even with the present value of the finesse.

In addition to these straightforward extensions to the present work, a number of other interesting possibilities arise. Sub-wavelength grating mirrors with focusing ability have been demonstrated [31], allowing the possibility of an all-grating cavity with no dielectric mirror, in which the mechanical motion of both gratings could be coupled by radiation pressure. It may be possible to make a grating giving high TE and TM reflectivities for different wavelengths, allowing a richer variety of ‘pump/probe’ experiments. It was recently suggested in a theoretical paper [32] that by designing a photonic crystal mirror with a rapidly varying reflectivity as a function of wavelength, it should be possible to engineer optomechanical damping and antidamping without the need for an optical cavity. Indeed, sub-wavelength gratings such as those studied here can be designed to have resonant features with a reflectivity that varies very rapidly from zero to unity as a function of wavelength [12], which may allow such phenomena to be observed. An interesting question that arises is whether the motion of individual fingers in the grating can be observed as well. In the present sample, the frequency of the fundamental finger mode is $\nu_1 \approx 1.8\ \text{MHz}$, at which point the density of membrane modes ν_{mn} is very high (mean spacing between modes $\approx 3\ \text{kHz}$). Thus, even if the motion of a finger were transduced by the cavity, the response would not be distinguishable from that of a membrane mode. The situation is vastly more favorable for a smaller membrane. In a square membrane with $a = 90\ \mu\text{m}$ and finger length $l = 50\ \mu\text{m}$, for example, the fundamental mode of a finger would fall midway between the $(m, n) = (1, 1)$ and $(m, n) = (1, 2)$ modes of the membrane, and thus would be easily identified.

Finally, there arises the interest in using these devices in a ‘membrane in the middle’ configuration. In such an application the grating size and cavity length should be less critical; the cavity length could be set far from the critical point so that the waist would be much larger, but any part of the spatial mode ‘spilling over’ the grating would still be confined to the cavity, and thus would not constitute a loss mechanism. Perhaps the most tantalizing possibility [6] is that in which the optomechanical coupling achievable by placing a small number of such gratings in a cavity would enable strong coupling between a single phonon and a single photon.

Acknowledgments

We acknowledge National Science Foundation support through the Physics Frontier Center at the Joint Quantum Institute. Research performed in part at the NIST Center for Nanoscale Science and Technology.

References

- [1] Kippenberg T J and Vahala K J 2007 Cavity opto-mechanics *Opt. Express* **15** 17172–205
- [2] Thompson J D, Zwickl B M, Jayich A M, Marquardt F, Girvin S M and Harris J G E 2008 Strong dispersive coupling of a high-finesse cavity to a micromechanical membrane *Nature* **452** 72–5
- [3] Wilson D J, Regal C A, Papp S B and Kimble H J 2009 Cavity optomechanics with stoichiometric SiN films *Phys. Rev. Lett.* **103** 207204
- [4] Hartmann M and Plenio M 2008 Steady state entanglement in the mechanical vibrations of two dielectric membranes *Phys. Rev. Lett.* **101** 200503
- [5] Bhattacharya M and Meystre P 2008 Multiple membrane cavity optomechanics *Phys. Rev. A* **78** 041801
- [6] Xuereb A, Genes C and Dantan A 2012 Strong coupling and long-range collective interactions in optomechanical arrays arXiv:1202.6210
- [7] Huang M C Y, Zhou Y and Chang-Hasnain C J 2007 A surface-emitting laser incorporating a high-index-contrast subwavelength grating *Nature Photon.* **1** 119–22
- [8] Antoni T *et al* 2011 Deformable two-dimensional photonic crystal slab for cavity optomechanics *Opt. Lett.* **36** 3434–6
- [9] Kemiktarak U, Metcalfe M, Durand M and Lawall J 2012 Mechanically compliant grating reflectors for optomechanics *Appl. Phys. Lett.* **100** 061124
- [10] Marquardt F, Chen J, Clerk A and Girvin S 2007 Quantum theory of cavity-assisted sideband cooling of mechanical motion *Phys. Rev. Lett.* **99** 093902
- [11] Wilson-Rae I, Nooshi N, Zwerger W and Kippenberg T 2007 Theory of ground state cooling of a mechanical oscillator using dynamical backaction *Phys. Rev. Lett.* **99** 093901
- [12] Chang-Hasnain C J 2011 High-contrast gratings as a new platform for integrated optoelectronics *Semicond. Sci. Technol.* **26** 014043
- [13] Sharon A, Rosenblatt D and Friesem A A 1997 Resonant grating-waveguide structures for visible and near-infrared radiation *J. Opt. Soc. Am. A* **14** 2985–93
- [14] Fan S and Joannopoulos J D 2002 Analysis of guided resonances in photonic crystal slabs *Phys. Rev. B* **65** 235112
- [15] Clausnitzer T, Kämpfe T, Kley E-B, Tünnermann A, Peschel U, Tishchenko A V and Parriaux O 2005 An intelligible explanation of highly-efficient diffraction in deep dielectric rectangular transmission gratings *Opt. Express* **13** 10448–56
- [16] Lalanne P, Hugonin J P and Chavel P 2006 Optical properties of deep lamellar gratings: a coupled Bloch-mode insight *J. Light. Technol.* **24** 2442–9
- [17] Karagodsky V, Sedgwick F and Chang-Hasnain C J 2010 Theoretical analysis of subwavelength high contrast grating reflectors *Opt. Express* **18** 16973–88
- [18] Chase C, Rao Y, Hofmann W and Chang-Hasnain C J 2010 1550 nm high contrast grating VCSEL *Opt. Express* **18** 15461–6
- [19] Brückner F, Friedrich D, Clausnitzer T, Britzger M, Burmeister O, Danzmann K, Kley E-B, Tünnermann A and Schnabel R 2010 Realization of a monolithic high-reflectivity cavity mirror from a single silicon crystal *Phys. Rev. Lett.* **104** 163903
- [20] Lousse V, Suh W, Kilic O, Kim S, Solgaard O and Fan S 2004 Angular and polarization properties of a photonic crystal slab mirror *Opt. Express* **12** 1575–82

- [21] Moharam M G and Gaylord T K 1981 Rigorous coupled-wave analysis of planar-grating diffraction *J. Opt. Soc. Am.* **71** 811–8
- [22] Germer T *MIST: Modeled Integrated Scatter Tool* version 3.01 (available at <http://pml.nist.gov/scatmech>)
- [23] Brückner F, Friedrich D, Clausnitzer T, Burmeister O, Britzger M, Kley E-B, Danzmann K, Tünnermann A and Schnabel R 2009 Encapsulated subwavelength grating as a quasi-monolithic resonant reflector *Opt. Express* **17** 24334–41
- [24] Jayich A M, Sankey J C, Zwickl B M, Yang C, Thompson J D, Girvin S M, Clerk A A, Marquardt F and Harris J G E 2008 Dispersive optomechanics: a membrane inside a cavity *New J. Phys.* **10** 095008
- [25] Mamin H J and Rugar D 2001 Sub-attoneutron force detection at millikelvin temperatures *Appl. Phys. Lett.* **79** 3358
- [26] Kogelnik H and Li T 1966 Laser beams and resonators *Proc. IEEE* **54** 1312–29
- [27] Kleckner D, Irvine W T M, Oemrawsingh S S R and Bouwmeester D 2010 Diffraction-limited high-finesse optical cavities *Phys. Rev. A* **81** 043814
- [28] Klaassen T, de Jong J, van Exter M and Woerdman J P 2005 Transverse mode coupling in an optical resonator *Opt. Lett.* **30** 1959–61
- [29] Hall J L, Ye J and Ma L S 2000 Measurement of mirror birefringence at the sub-ppm level: proposed application to a test of QED *Phys. Rev. A* **62** 013815
- [30] Timoshenko S 1937 *Vibration Problems in Engineering* (New York: Van Nostrand)
- [31] Lu F, Sedgwick F, Karagodsky V, Chase C and Chang-Hasnain C J 2010 Planar high-numerical-aperture low-loss focusing reflectors and lenses using subwavelength high contrast gratings *Opt. Express* **18** 12606–14
- [32] Karrai K, Favero I and Metzger C 2008 Doppler optomechanics of a photonic crystal *Phys. Rev. Lett.* **100** 240801